Case Studies in Thermal Engineering 66 (2025) 105768

Contents lists available at ScienceDirect

Case Studies in Thermal Engineering

journal homepage: www.elsevier.com/locate/csite

Mixed convection hybrid nanofluid flow past a non-isothermal cone and wedge with radiation and convective boundary condition: Heat transfer optimization

Rusya Iryanti Yahaya [a], Norihan Md Arifin [a,b,*], Mohd Shafie Mustafa [b], Ioan Pop [c], Fadzilah Md Ali [a,b], Siti Suzilliana Putri Mohamed Isa [a,d]

[a] Institute for Mathematical Research, Universiti Putra Malaysia, UPM Serdang, 43400, Selangor, Malaysia
[b] Department of Mathematics and Statistics, Universiti Putra Malaysia, UPM Serdang, 43400, Selangor, Malaysia
[c] Department of Mathematics, Babeş-Bolyai University, 400084, Cluj-Napoca, Romania
[d] Centre for Foundation Studies in Science of Universiti Putra Malaysia, Universiti Putra Malaysia, UPM Serdang, 43400, Selangor, Malaysia

ARTICLE INFO

Keywords:
Hybrid nanofluid
Mixed convection
Non-isothermal
Cone/wedge
RSM

ABSTRACT

This study analyzes the steady hybrid nanofluid flow over a permeable, non-isothermal cone and wedge. The heat transfer analysis considers the effects of thermal radiation and convective boundary conditions. Non-linear ordinary differential equations, derived through similarity transformation of the governing partial differential equations and boundary conditions, are solved numerically using the bvp4c solver. The resulting triple solutions are then subjected to a stability analysis. It is confirmed that only the first solution is stable and physically meaningful, while the other solutions are unstable. The physical quantities of interest, namely the local skin friction coefficient and local Nusselt number, are found to be higher for assisting mixed convection flow than for opposing flow. Compared to the wedge geometry, hybrid nanofluid flow over the cone exhibits a lower local skin friction coefficient but a higher local Nusselt number. Furthermore, optimization results from the response surface methodology (RSM) indicate that the maximum local Nusselt number, corresponding to the highest heat transfer rate at the cone/wedge surface, can be achieved at high values of the Biot number, radiation parameter, and wall temperature parameter.

Nomenclature

ρ	Density (kg/m^3)	x,y	Cartesian coordinates (m)
τ	Dimensionless time variable	A, B, C	Coded independent variables
ψ	Stream function	Bi	Biot number
λ	Mixed convection parameter	c_0	Intercept term
γ	Unknown eigenvalue	c_i	Linear term
k	Thermal conductivity (W/m K)	cii	Quadratic term
C_p	Heat capacity (J/kg K)	c_{ij}	Bilinear two-factor term
β	Thermal expansion coefficient	C_f	Local skin friction coefficient
α	Half-angle of the cone/wedge	Er	Statistical error

(*continued on next page*)

* Corresponding author. Institute for Mathematical Research, Universiti Putra Malaysia, UPM Serdang, 43400, Selangor, Malaysia.
E-mail address: norihana@upm.edu.my (N. Md Arifin).

https://doi.org/10.1016/j.csite.2025.105768
Received 26 June 2023; Received in revised form 20 December 2024; Accepted 6 January 2025
Available online 8 January 2025

(*continued*)

μ	Dynamic viscosity (kg/m s)	f	Dimensionless velocity
η	Similarity variable	g	Acceleration due to gravity (m/s^2)
ν	Kinematic viscosity (m^2/s)	Gr_x	Local Grashof number
a	Constant	h_f	Heat transfer coefficient
θ	Dimensionless temperature	hnf	Hybrid nanofluid
σ^*	Stefan-Boltzmann constant	k^*	Mean absorption coefficient
ϕ	Nanoparticle volume fraction	l	Characteristic length of cone/wedge
Nu_x	Local Nusselt number	N	Number of independent variables
n	Cone/wedge geometry	q_r	Radiative heat flux
P	Center point	s_1	Wall temperature parameter
r	Radius (m)	Pr	Prandtl number
Rd	Radiation parameter	t	Time (s)
Re_x	Local Reynolds number	S	Suction parameter
T_f	Convective heating temperature (K)	u, v	Velocity components (m/s)
v_w	Mass transfer velocity (m/s)	T_∞	Ambient fluid temperature

1. Introduction

Nanofluid is a heat transfer fluid containing the suspension of a single type nanoparticle in a base fluid. Researchers have analyzed the flow and thermal behaviors of various nanofluids in different flow configurations (see Refs. [1–6]). Meanwhile, a hybrid nanofluid comprises the dispersion of two or more distinct nanoparticles in a heat transfer fluid such as water, oil, or ethylene glycol. There have been several scientific discussions about the preparation, correlation of thermophysical properties, and applications of hybrid nanofluids (see Refs. [7–12]). Additionally, research has been conducted on the boundary layer flow of hybrid nanofluids over various physical geometries subjected to a wide range of conditions. For example, hybrid nanofluid flow over a stretching/shrinking sheet has been analyzed due to its wide range of applications in paper production, the extrusion of plastics, and the creation of rubber sheets [13]. Yashkun et al. [14] scrutinized the impacts of magnetic field and thermal radiation on hybrid nanofluid flow over a permeable stretching/shrinking sheet. It was found that Cu/H_2O nanofluid had a lower heat transfer performance than the Al_2O_3-Cu/H_2O hybrid nanofluid. Asghar et al. [15] discussed the three-dimensional flow over a rotating stretching/shrinking sheet with Joule heating. Dual solutions were found for the shrinking sheet case. In contrast, a single solution was obtained for the stretching sheet case over various values of the magnetic parameter and Cu nanoparticle volume fraction. Similar results were reported by Mousavi et al. [16], where the stability analysis determined that only one solution was stable. Then, Mahabaleshwar et al. [17] investigated the flow over a stretching/shrinking sheet with thermal radiation and mass transpiration. Contrary to the mass transpiration parameter, the increase in the radiation parameter enhanced the thermal boundary layer thickness. Muhammad et al. [18] analyzed the Darcy-Forchheimer flow of a hybrid nanofluid over a curved stretching surface. It was observed that an increase in the curvature parameter reduced the local skin friction coefficient, while the local Nusselt number increased with the volume fraction of nanoparticles. Other studies on hybrid nanofluid flow over stretching/shrinking sheets have also been carried out by Nadeem et al. [13] and Vishalakshi et al. [19]. Next, there were also studies on hybrid nanofluid flow over a disk (see Refs. [20–25]). The flow over a disk has several engineering applications, including rotating machinery, chemical processes, gas turbine rotators, computer storage, and the geothermal industry [20]. Some researchers have considered hybrid nanofluid flow over multiple geometries. Sulochana et al. [26] discussed hybrid nanofluid flow past cone and wedge geometries. This flow type is relevant for real-life applications involving solar power collectors, spacecraft design, nuclear reactors, steam generators, and power transformers. It was discovered from this study that the heat transfer rate was greater past the cone than the wedge. Haq et al. [27] then analyzed the flow over three distinct geometries of plate, wedge, and cone with homogeneous-heterogeneous effects and reported similar conclusions to Sulochana et al. [26]. Meanwhile, Rekha et al. [28] found that incrementing the heat source/sink parameter improved heat transfer across the plate, but the opposite occurred for the cone and wedge. Al-Arabi et al. [29] considered the effects of different nanoparticle shapes in hybrid nanofluid flow over a cone/wedge. Other recent works on hybrid nanofluid flow across plate, cone, and wedge are also interesting to ponder (see Refs. [30–34]).

Non-isothermal refers to a condition where the temperature is neither uniform nor constant. It may arise in cooling metallic plates, thin-film solar energy collector devices, microelectromechanical (MEM) condensation applications, and aerodynamic extrusion of plastic sheets [35]. Meanwhile, non-isosolutal denotes a condition with non-uniform solute concentration. Chen [36] studied the heat transfer between a non-isothermal surface and a fluid. For this study, the temperature of the surface was supposed to fluctuate according to power law. The increase in the non-isothermal behavior through the wall temperature parameter was found to boost the heat transfer rate. Then, Kumari et al. [37] analyzed the flow of power-law fluids across a non-isothermal surface. Ray et al. [38] and Dawar et al. [39] considered nanofluid flow past non-isothermal, non-isosolutal multiple geometries of plate, cone, and wedge. In these studies, enhancing the non-isothermal (i.e., wall temperature parameter) and non-isosolutal (i.e., wall concentration parameter) effects reduced the temperature and concentration profiles. In recent years, Bilal et al. [40] discussed the flow of Williamson fluid over a non-isothermal exponential surface. It was observed that the increment of the wall temperature parameter reduced the temperature profile. In the meantime, there were studies on the flow of nanofluid and hybrid nanofluid across non-isothermal surfaces. Then, Waini et al. [35] examined the hybrid nanofluid flow past a non-isothermal shrinking surface. This investigation concluded that the isothermal surface transferred heat more quickly than the non-isothermal surface. Meanwhile, Nithya and Vennila [41] extended this study by incorporating the effects of heat source/sink. Recently, Ramzan et al. [42] investigated the flow of a ternary hybrid nanofluid over non-isothermal, non-isosolutal cone and wedge geometries. Again, a decrement in the profiles of concentration and temperature

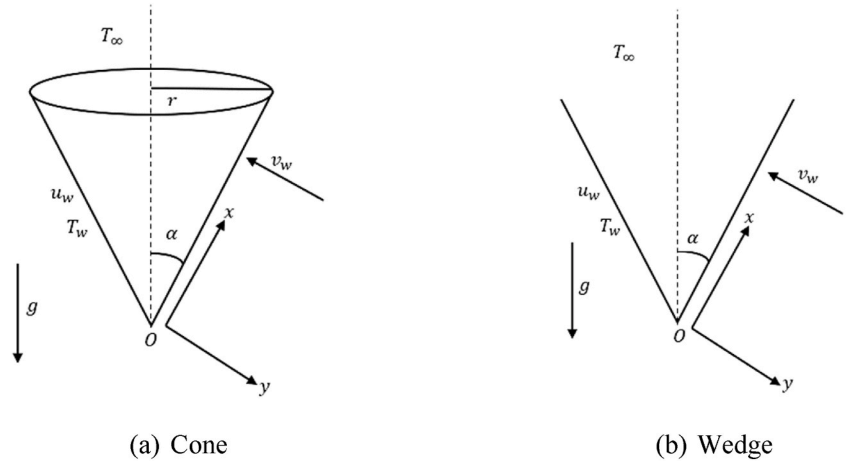

Fig. 1. Physical model and coordinate system.

was seen with the increasing value of the wall concentration and temperature parameters.

Based on the previous studies, we aim to analyze the mixed convection boundary layer flow of hybrid nanofluid past permeable, non-isothermal cone and wedge. This flow problem will be represented by governing equations and boundary conditions. In addition, the effects of thermal radiation and convective boundary condition will be introduced into the energy equation and boundary condition, respectively. A numerical investigation will be conducted using the bvp4c solver, and statistical analysis will be performed using the response surface methodology (RSM) to identify optimal conditions for effective heat transfer. Combining the numerical and statistical investigations will provide a better understanding of the results. Since no other researchers have addressed the current flow problem, this study may help fill the literature gap.

2. Mathematical model

Heat exchangers are frequently used in cooling processes across various applications, including solar thermal systems, power plants, and industrial high-temperature operations. These exchangers may feature complex geometries, such as cones and wedges with permeable surfaces. Hybrid nanofluids may be employed as the working fluid, and factors such as non-isothermal effects, mixed convection, thermal radiation, and convective boundary condition may also arise. Analyzing the flow and thermal behaviors of hybrid nanofluids under these conditions offers valuable insights for enhancing and optimizing heat transfer performance.

Hence, this study analyzes the mixed convection hybrid nanofluid flow past a vertical, non-isothermal, permeable cone/wedge through numerical and statistical investigations. The heat transfer fluid is a water-based (H_2O) hybrid nanofluid containing two different nanoparticles: alumina (Al_2O_3) and copper (Cu). It is assumed that:

i. The nanoparticles have a uniform size and shape and are in a thermal equilibrium state.
ii. The base fluid and the suspended nanoparticles are in thermal equilibrium.

Fig. 1 depicts the geometry and coordinates system of the two-dimensional flow problem with $x-$ and $y-$ axes measured parallel and normal to the cone/wedge surface, respectively. The flow is assumed to occupy the region $y \geq 0$, and the temperature of the cone/wedge is $T_f(x) = T_\infty + ax^{s_1}$. Here, T_∞ is the ambient temperature, a is a constant, and s_1 is the wall temperature parameter, with $s_1 = 0$ denoting isothermal (i.e., constant wall temperature). The surface of the cone/wedge is assumed to be permeable with v_w as the mass transfer velocity where $v_w < 0$ for suction and $v_w > 0$ for injection. The cone/wedge has a half-angle of α, and the radius of the cone is $r(= x \sin \alpha)$. Meanwhile, the radiative heat flux and convective heat transfer coefficient are given by q_r and h_f, respectively.

The governing boundary layer equations for the flow problem consist of the following mass, momentum, and energy equations [42]:

$$\frac{\partial(r^n u)}{\partial x} + \frac{\partial(r^n v)}{\partial y} = 0, \tag{1}$$

$$u\,\frac{\partial u}{\partial x} + v\,\frac{\partial u}{\partial y} = \frac{\mu_{hnf}}{\rho_{hnf}}\,\frac{\partial^2 u}{\partial y^2} + g\left[\beta_{hnf}(T - T_\infty)\right]\cos\alpha, \tag{2}$$

$$u\,\frac{\partial T}{\partial x} + v\,\frac{\partial T}{\partial y} = \frac{k_{hnf}}{(\rho\, C_p)_{hnf}}\,\frac{\partial^2 T}{\partial y^2} - \frac{1}{(\rho C_p)_{hnf}}\,\frac{\partial q_r}{\partial y}, \tag{3}$$

Table 1
Thermophysical properties of H_2O, Al_2O_3, and Cu [45,46].

Base fluid/nanoparticles	$\rho\ (kg/m^3)$	$C_p (J/kgK)$	$k\ (W/mK)$	$\beta\ (1/K)$
H_2O (base fluid)	997.1	4179	0.613	$21 \cdot 10^{-5}$
Al_2O_3	3970	765	40	$0.85 \cdot 10^{-5}$
Cu	8933	385	400	$1.67 \cdot 10^{-5}$

with the boundary conditions [42,43]:

$$\left.\begin{aligned} v = v_w, u = u_w = \frac{\nu_{H_2O} x}{l^2}, -k_{hnf}\frac{\partial T}{\partial y} = h_f\left(T_f - T\right) \text{ at } y = 0 \\ u \to 0, T \to T_\infty \text{ as } \quad y \to \infty \end{aligned}\right\}. \tag{4}$$

In Eq. (1)

i. $n = 0, \alpha \neq 0$ refers to the wedge geometry.
ii. $n = 1, \alpha \neq 0$ refers to the cone geometry.

Meanwhile, g is the acceleration due to gravity, (u, v) is the velocity component along the $(x, y)-$ axis, T is the hybrid nanofluid temperature, ν_{H_2O} is the kinematic viscosity of water, and l is the characteristic length of the cone/wedge.

Further, the correlations for the dynamic viscosity $\left(\mu_{hnf}\right)$, density (ρ_{hnf}), thermal conductivity (k_{hnf}), heat capacity $(\rho C_p)_{hnf}$, and thermal expansion coefficient $\left(\beta_{hnf}\right)$ of the hybrid nanofluid are given by Ref. [44]:

$$\left.\begin{aligned} &\mu_{hnf} = \mu_{H_2O}\left(1 - \phi_{hnf}\right)^{-2.5}, \\ &\rho_{hnf} = \phi_{Al_2O_3}\rho_{Al_2O_3} + \phi_{Cu}\rho_{Cu} + \left(1 - \phi_{hnf}\right)\rho_{H_2O}, \\ &\frac{k_{hnf}}{k_{H_2O}} = \left\{\frac{\phi_{Al_2O_3}k_{Al_2O_3} + \phi_{Cu}k_{Cu}}{\phi_{Al_2O_3} + \phi_{Cu}} + 2k_{H_2O} + 2(\phi_{Al_2O_3}k_{Al_2O_3} + \phi_{Cu}k_{Cu}) - 2(\phi_{Al_2O_3} + \phi_{Cu})k_{H_2O}\right\} \times \\ &\left\{\frac{\phi_{Al_2O_3}k_{Al_2O_3} + \phi_{Cu}k_{Cu}}{\phi_{Al_2O_3} + \phi_{Cu}} + 2k_{H_2O} - (\phi_{Al_2O_3}k_{Al_2O_3} + \phi_{Cu}k_{Cu}) + (\phi_{Al_2O_3} + \phi_{Cu})k_{H_2O}\right\}^{-1}, \\ &(\rho C_p)_{hnf} = \phi_{Al_2O_3}(\rho C_p)_{Al_2O_3} + \phi_{Cu}(\rho C_p)_{Cu} + \left(1 - \phi_{hnf}\right)(\rho C_p)_{H_2O}, \\ &(\rho\beta)_{hnf} = \left(1 - \phi_{hnf}\right)(\rho\beta)_{H_2O} + \phi_{Al_2O_3}(\rho\beta)_{Al_2O_3} + \phi_{Cu}(\rho\beta)_{Cu}, \end{aligned}\right\},$$

where ϕ refers to nanoparticle volume fraction and $\phi_{hnf} = \phi_{Al_2O_3} + \phi_{Cu}$. The thermophysical properties of the base fluid and nanoparticles are listed in Table 1.

According to Rosseland's [47] approximation, the radiative heat flux q_r can be expressed as follows [48–50]:

$$q_r = -\frac{4\,\sigma^*}{3\,k^*}\frac{\partial T^4}{\partial y}, \tag{6}$$

where k^* and σ^* denote the mean absorption coefficient and Stefan-Boltzmann constant, respectively. Using the Taylor series and ignoring higher-order terms, T^4 is expanded about T_∞ to obtain $T^4 \approx 4T_\infty^3 T - 3T_\infty^4$. Equation (3) can now be written as:

$$u\frac{\partial T}{\partial x} + v\frac{\partial T}{\partial y} = \frac{1}{(\rho\, C_p)_{hnf}}\left(k_{hnf} + \frac{16\,\sigma^*\,T_\infty^3}{3\,k^*}\right)\frac{\partial^2 T}{\partial y^2}. \tag{7}$$

Next, the following similarity variables are introduced [42]:

$$u = \left(\nu_{H_2O}\frac{x}{l^2}\right)f'(\eta), v = -\left(\frac{\nu_{H_2O}}{l}\right)(1+n)f(\eta), \theta(\eta) = \frac{T - T_\infty}{T_f - T_\infty}, \eta = y\Big/l, \tag{8}$$

with the prime $(')$ denotes differentiation with respect to η. Substituting the similarity variables (8) into equations (2), (4) and (7) reduces the equations into the following ordinary differential equations:

$$\frac{\mu_{hnf}\big/\mu_{H_2O}}{\rho_{hnf}\big/\rho_{H_2O}} f''' + (1+n)f f'' - f'^2 + \lambda\left(\frac{\beta_{hnf}}{\beta_{H_2O}}\cos\alpha\right)\theta = 0, \tag{9}$$

$$\frac{1}{Pr}\frac{1}{(\rho C_p)_{hnf}\Big/(\rho C_p)_{H_2O}}\left(\frac{k_{hnf}}{k_{H_2O}}+\frac{4}{3}Rd\right)\theta^{''}+(1+n)f\theta^{'}-s_1f^{'}\theta=0. \tag{10}$$

The boundary conditions then become:

$$\left.\begin{array}{c} f(0)=\dfrac{S}{1+n}, f^{'}(0)=1, \theta^{'}(0)=-\dfrac{k_{H_2O}}{k_{hnf}}Bi[1-\theta(0)], \\ f^{'}(\eta)\to 0, \theta(\eta)\to 0 \ \text{ as } \ \eta\to\infty, \end{array}\right\}. \tag{11}$$

In the above equations, $\lambda\left(=Gr_x/Re_x^2\right)$ is the mixed convection parameter with $Gr_x\left(=\frac{g\beta_{H_2O}(T_f-T_\infty)x^3}{\nu_{H_2O}^2}\right)$ as the local Grashof number and $Re_x\left(=x^2/l^2\right)$ as the local Reynolds number, $Pr\left(=\frac{(\mu C_p)_{H_2O}}{k_{H_2O}}\right)$ is the Prandtl number, $Rd\left(=\frac{4\sigma^* T_\infty^3}{k_{H_2O}k^*}\right)$ is the radiation parameter, $S\left(=-\frac{l v_w}{\nu_{H_2O}}\right)$ is the suction parameter with $S>0$, and $Bi\left(=\frac{h_f l}{k_{H_2O}}\right)$ is the Biot number. It should also be noticed that $\lambda>0$ corresponds to the assisting flow, $\lambda<0$ is for the opposing flow, and $\lambda=0$ corresponds to the forced convection flow.

Finally, the physical quantities of interest are the local Nusselt number (Nu_x) and local skin friction coefficient (C_f), which are defined as [42]:

$$Nu_x=-\frac{x}{k_{H_2O}(T_f-T_\infty)}\left[\left(k_{hnf}\frac{\partial T}{\partial y}\right)_{y=0}-(q_r)_{y=0}\right], C_f=\frac{\mu_{hnf}}{\rho_{H_2O}u_w^2}\left(\frac{\partial u}{\partial y}\right)_{y=0}. \tag{12}$$

By substituting the similarity variables (8) into (12):

$$Re_x^{\frac{1}{2}}C_f=\frac{\mu_{hnf}}{\mu_{H_2O}}f''(0),\ Re_x^{-\frac{1}{2}}Nu_x=-\left(\frac{k_{hnf}}{k_{H_2O}}+\frac{4}{3}Rd\right)\theta^{'}(0). \tag{13}$$

3. Stability analysis of solutions

The boundary value problem (9) to (11) presented in the previous section will be solved in MATLAB using bvp4c, a finite difference code-containing solver. Multiple solutions may arise during the numerical computation that prompts a stability analysis. Following Merkin [51], the stability analysis selects the stable and meaningful solution among the obtained multiple solutions. The current boundary value problem (2) and (3) is reintroduced as the following time-dependent equations:

$$\frac{\partial u}{\partial t}+u\frac{\partial u}{\partial x}+v\frac{\partial u}{\partial y}=\frac{\mu_{hnf}}{\rho_{hnf}}\frac{\partial^2 u}{\partial y^2}+g\left[\beta_{hnf}(T-T_\infty)\right]\cos\alpha, \tag{14}$$

$$\frac{\partial T}{\partial t}+u\frac{\partial T}{\partial x}+v\frac{\partial T}{\partial y}=\frac{k_{hnf}}{(\rho C_p)_{hnf}}\frac{\partial^2 T}{\partial y^2}-\frac{1}{(\rho C_p)_{hnf}}\frac{\partial q_r}{\partial y}, \tag{15}$$

with similarity variables containing dimensionless time variable (τ) and t as time:

$$\left.\begin{array}{c} u=\left(\nu_{H_2O}x/l^2\right)\dfrac{\partial}{\partial\eta}f(\eta,\tau), v=-(\nu_{H_2O}/l)(1+n)f(\eta,\tau) \\ \theta(\eta,\tau)=\dfrac{T-T_\infty}{T_f-T_\infty}, \eta=y\Big/l, \tau=\nu_{H_2O}t\Big/l^2 \end{array}\right\}. \tag{16}$$

Then, the similarity variables (16) are substituted into equations (14) and (15) to obtain:

$$\frac{\mu_{hnf}/\mu_{H_2O}}{\rho_{hnf}/\rho_{H_2O}}\frac{\partial^3 f}{\partial\eta^3}+(1+n)f\frac{\partial^2 f}{\partial\eta^2}-\left(\frac{\partial f}{\partial\eta}\right)^2+\lambda\left[\frac{\beta_{hnf}}{\beta_{H_2O}}\cos\alpha\right]\theta-\frac{\partial^2 f}{\partial\eta\partial\tau}=0, \tag{17}$$

$$\frac{1}{Pr}\frac{1}{(\rho C_p)_{hnf}\Big/(\rho C_p)_{H_2O}}\left(\frac{k_{hnf}}{k_{H_2O}}+\frac{4}{3}Rd\right)\frac{\partial^2\theta}{\partial\eta^2}+(1+n)f\frac{\partial\theta}{\partial\eta}-s_1\theta\frac{\partial f}{\partial\eta}-\frac{\partial\theta}{\partial\tau}=0, \tag{18}$$

with the boundary conditions of:

$$\left.\begin{array}{c} f(0,\tau)=\dfrac{S}{1+n}, f^{'}(0,\tau)=1, \theta^{'}(0,\tau)=-\dfrac{k_{H_2O}}{k_{hnf}}Bi[1-\theta(0,\tau)], \\ f^{'}(\eta,\tau)\to 0, \theta(\eta,\tau)\to 0 \ \text{ as } \ \eta\to\infty, \end{array}\right\}. \tag{19}$$

Table 2
Comparison of results for $-f''(0)$ when $\phi_{Al_2O_3} = \phi_{Cu} = n = \lambda = Rd = 0$ and $Bi = 10^6$

Pr	α	s_1	S	$-f''(0)$	
				Present study	Hassanien et al. [54]
6.2	1	1	1	1.61803	1.618034
			0.5	1.28078	1.280777
			−0.5	0.78078	0.780781
			0	1.00001	1.00000

Table 3
Comparison of results for $-\theta'(0)$ when $\phi_{Al_2O_3} = \phi_{Cu} = n = \lambda = Rd = 0$ and $Bi = 10^6$

Pr	α	s_1	S	$-\theta'(0)$	
				Present study	Waini et al. [55]
1	0	0	0	0.58201	0.5820
		1		1.00001	1.0000
		2		1.33333	1.3333
0.72		1		0.80864	0.8086
3				1.92368	1.9237

Table 4
Smallest eigenvalue (γ_1) for $Pr = 6.2, S = Bi = 0.5, \phi_{Al_2O_3} = \phi_{Cu} = 0.02, Rd = s_1 = 1.5,$ and $\alpha = \pi/4$

n	λ	γ_1		
		First solution	Second solution	Third solution
0	−0.5	0.84687	−0.22605	−0.23455
	0.5	0.61431	−0.22414	−0.23289
1	−0.5	1.49198	−0.22703	−0.23995
	0.5	1.47166	−0.22588	−0.23873

Next, the following perturbation functions are introduced [52]:

$$\left.\begin{aligned} f(\eta,\tau) &= f_0(\eta) + e^{-\gamma\tau}F(\eta,\tau), \\ \theta(\eta,\tau) &= \theta_0(\eta) + e^{-\gamma\tau}G(\eta,\tau), \end{aligned}\right\}, \tag{20}$$

which contains $F(\eta,\tau)$ and $G(\eta,\tau)$ as disturbances that grow or decay with time. Meanwhile, γ is the unknown eigenvalue, and $f_0(\eta)$ and $\theta_0(\eta)$ are the steady solutions that are relatively larger than the disturbances and their derivatives. These functions are then substituted into equations (17)–(19). The initial growth or decay of the disturbance can be analyzed by setting $\tau = 0$. Hence, the following linearized eigenvalue problem is obtained:

$$\frac{\mu_{hnf}/\mu_{H_2O}}{\rho_{hnf}/\rho_{H_2O}} F_0''' + (1+n)\left[f_0F_0'' + F_0f_0''\right] - 2f_0'F_0' + \lambda\left[\frac{\beta_{hnf}}{\beta_{H_2O}}\cos\alpha\right]G_0 + \gamma F_0' = 0, \tag{21}$$

$$\frac{1}{Pr}\frac{1}{(\rho C_p)_{hnf}/(\rho C_p)_{H_2O}}\left(\frac{k_{hnf}}{k_{H_2O}} + \frac{4}{3}Rd\right)G_0'' + (1+n)\left[f_0G_0' + F_0\theta_0'\right] - s_1\theta_0F_0' - s_1G_0f_0' + \gamma G_0 = 0, \tag{22}$$

$$\left.\begin{aligned} &F_0(0) = 0, F_0'(0) = 0, G_0'(0) = \frac{k_{H_2O}}{k_{hnf}}BiG_0(0), \\ &\quad F_0'(\eta)\to 0, G_0(\eta)\to 0 \ \text{as} \ \ \eta\to\infty, \end{aligned}\right\}. \tag{23}$$

To compute the range of possible eigenvalues using the bvp4c solver, one of the free stream boundary conditions (i.e., as $\eta\to\infty$) in (23) is relaxed. Hence, we have the following:

$$\left.\begin{aligned} &F_0(0) = 0, F_0'(0) = 0, F_0''(0) = 1, G_0'(0) = \frac{k_{H_2O}}{k_{hnf}}BiG_0(0), \\ &\qquad G_0(\eta)\to 0 \ \text{as} \ \ \eta\to\infty, \end{aligned}\right\}. \tag{24}$$

As stated by Awaludin et al. [53], the smallest eigenvalue (γ_1) determines the stability and significance of the solutions. The positive value of γ_1 denotes an initial decay of disturbance for a stable and meaningful solution, while the opposite is true for $\gamma_1 < 0$. Therefore, the value of γ_1 for each solution will be determined by solving equations (21) and (22) subject to the new boundary conditions (24).

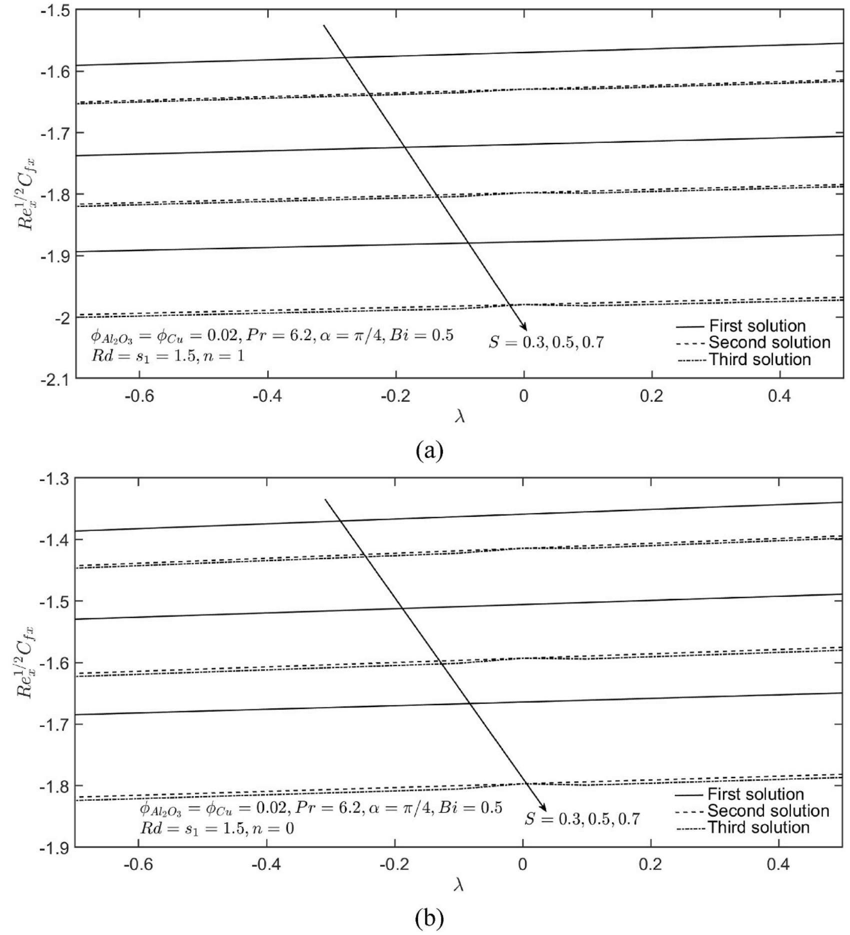

Fig. 2. Profiles of local skin friction coefficient $\left(Re_x^{\frac{1}{2}}C_f\right)$ for (a) cone and (b) wedge with various values of suction and mixed convection parameters.

4. Method of solution

All numerical results for this study are computed using the bvp4c solver. The syntax of the bvp4c solver is given by:

sol = bvp4c(@OdeBVP, @OdeBC, solinit, options).

Here, @OdeBVP is a function handle that defines the differential equations, @OdeBC specifies the boundary conditions, solinit is a structure containing the initial guesses, and options is an optional argument that holds the integration settings.

To allow computation using the bvp4c solver, equations (9)–(11) must be rewritten as first-order ordinary differential equations. Thus, the following substitutions are made:

$$f = y(1),\ f' = y(2), f'' = y(3), f''' = y(3)' = \frac{\left[-(1+n)y(1)y(3) + (y(2))^2 - \lambda\left(\frac{\beta_{hnf}}{\beta_{H_2O}}\cos\alpha\right)y(4)\right]}{\left[\frac{\mu_{hnf}/\mu_{H_2O}}{\rho_{hnf}/\rho_{H_2O}}\right]}, \tag{25}$$

$$\theta = y(4), \theta' = y(5), \theta'' = y(5)' = \frac{[-(1+n)y(1)y(5) + s_1 y(2)y(4)]}{\left[\left(\frac{1}{Pr}\frac{k_{hnf}/k_{H_2O}}{(\rho\ C_p)_{hnf}\Big/(\rho\ C_p)_{H_2O}}\right)\left(\frac{k_{hnf}}{k_{H_2O}} + \frac{4}{3}Rd\right)\right]}, \tag{26}$$

$$ya(1) = \frac{S}{1+n}, ya(2) = 1, ya(5) = -\frac{k_{H_2O}}{k_{hnf}}Bi[1 - ya(4)] \quad \text{at} \quad \eta = 0, \tag{27}$$

$$yb(2) \to 0, yb(4) \to 0 \text{ as } \eta \to \infty. \tag{28}$$

Then, two codes, called Code A and Code B, are employed to solve equations (25)–(28). Code A contains the main algorithm for

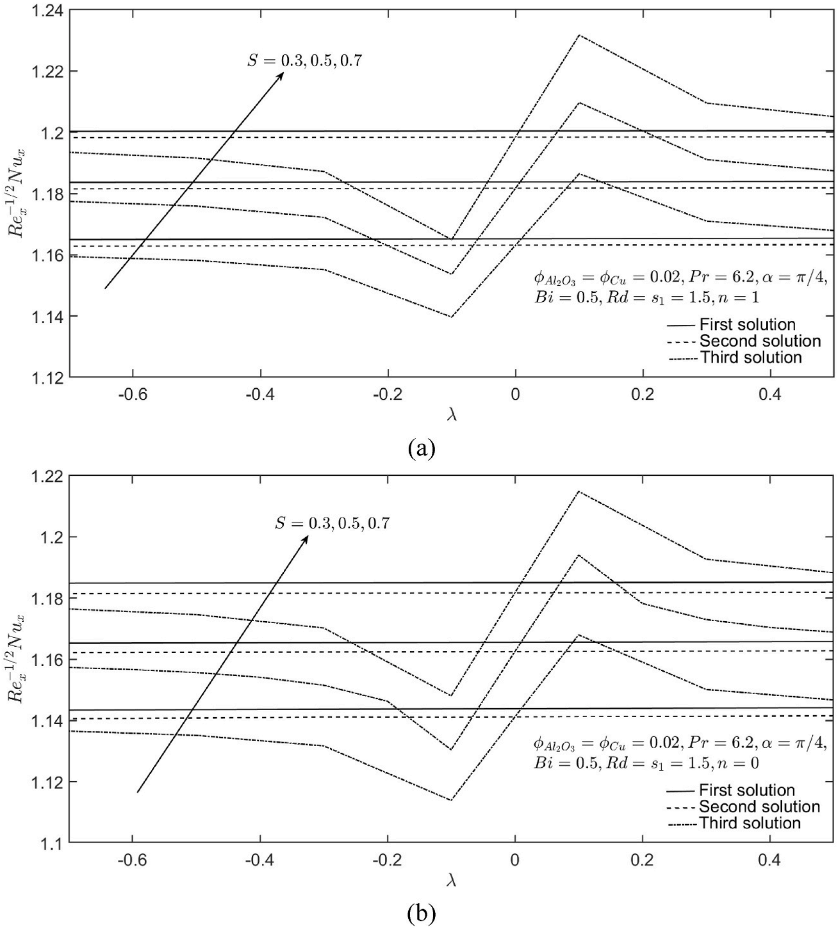

Fig. 3. Profiles of local Nusselt number $\left(Re_x^{-\frac{1}{2}} Nu_x\right)$ for (a) cone and (b) wedge with various values of suction and mixed convection parameters.

solving the boundary value problem. In this code, equations (25) and (26) are defined in @OdeBVP, while the boundary conditions (27) and (28) are coded into @OdeBC. Initial guesses for the solutions are then provided in solinit. These guesses are determined through trial and error until solutions that asymptotically satisfy the free stream boundary conditions (11) are achieved. Determining an initial guess for the first solution is relatively straightforward, as the bvp4c solver can converge to the first solution even with less accurate guesses. However, finding accurate initial guesses for the second and third solutions is more challenging. Therefore, the continuation technique [43] is utilized to address this challenge. Code B serves as the continuation code that overcomes the difficulty of making initial guesses by solving the boundary value problem using the initial guesses made in Code A.

In addition, equations (21) and (22), along with the boundary conditions (24), are rewritten as a system of first-order ordinary differential equations using the following substitutions:

$$F_0 = y(1), F_0' = y(2), F_0'' = y(3), G_0 = y(4), G_0' = y(5),$$

$$f_0 = s(1), f_0' = s(2), f_0'' = s(3), \theta_0 = s(4), \theta_0' = s(5).$$

The stability analysis is then conducted using Code C, Code D, and Code E in the bvp4c solver. These codes analyze the stability of the solutions by computing the smallest eigenvalue γ_1 for equations (21) and (22) subject to the boundary conditions (24). Specifically, Code C, Code D, and Code E are designed to compute γ_1 for the first, second, and third solutions, respectively. However, to ensure proper execution, these codes must be run sequentially in the following order: Code A, Code B, Code C, Code D, and Code E.

5. Results and discussion

The bvp4c solver numerically solves the boundary value problem (9) to (11). Tables 2 and 3 compare the present results with those reported by Hassanien et al. [54] and Waini et al. [55]. The published results were computed using the expansion of Chebyshev polynomials and the bvp4c solver, respectively. The excellent agreement between the present and published results validates the

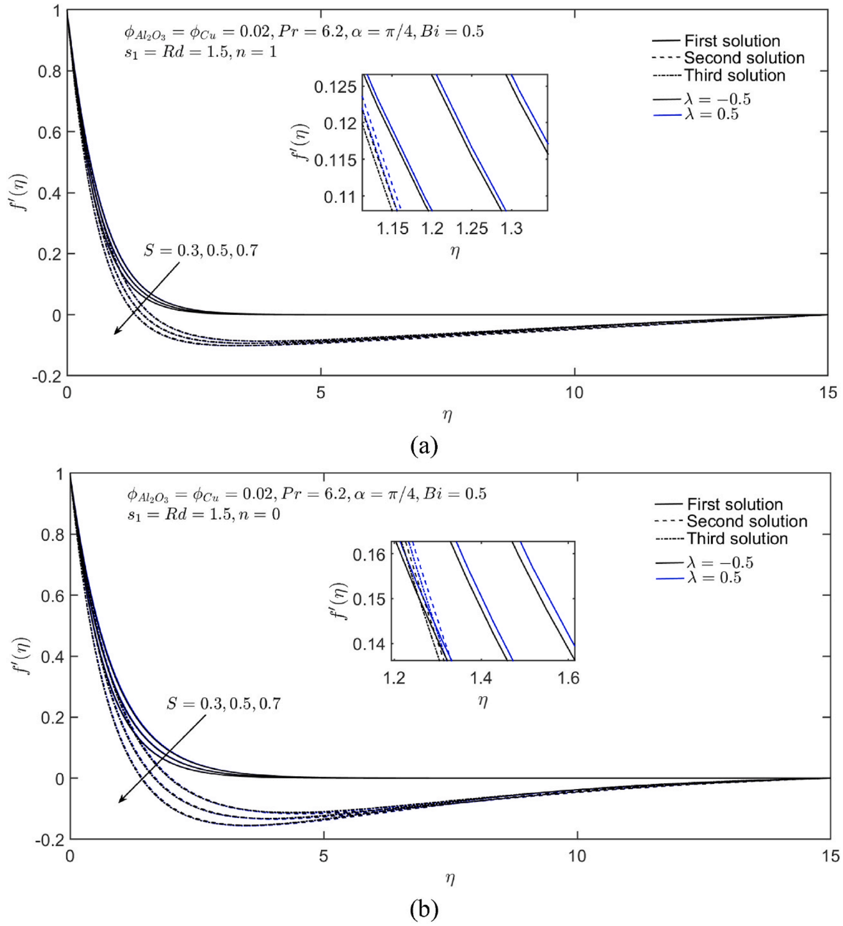

Fig. 4. Velocity profiles for (a) cone and (b) wedge with varying values of the suction parameter.

approach adopted in the current study and provides confidence in the reliability of the numerical results.

The boundary value problem (9) to (11) may possess no solution, single solution, or multiple solutions. An excellent initial guess must be made to generate the correct solution that satisfies the free stream boundary conditions asymptotically. In the present study, multiple solutions are obtained for different sets of initial guesses. The solutions are referred to as the first, second, and third based on their arrival at the free stream boundary conditions (11). All solutions are recorded in this study, but the discussion will only encompass the stable and meaningful solution. Hence, stability analysis is conducted to identify the stable solution. The results of the smallest eigenvalue are tabulated in Table 4. The first solution is stable due to the positive value of γ_1, whereas the second and third solutions are unstable as $\gamma_1 < 0$.

Figs. 2 and 3 display the profiles for physical quantities of interest $\left(\text{i.e.}, Re_x^{\frac{1}{2}}C_f \text{ and } Re_x^{-\frac{1}{2}}Nu_x\right)$ with various values of suction (S) and mixed convection (λ) parameters. Based on these figures, triple solutions exist at certain values of the mixed convection parameter. In addition, the local skin friction coefficient $\left(Re_x^{\frac{1}{2}}C_f\right)$ for both assisting and opposing flows over the cone and wedge decreases as the suction parameter increases (see Fig. 2). However, the increment of $Re_x^{\frac{1}{2}}C_f$, which is related to the wall shear stress, is seen with the increase in the mixed convection parameter. In Fig. 3, the local Nusselt number $\left(Re_x^{-\frac{1}{2}}Nu_x\right)$, which is related to the heat transfer rate at the wall, rises with the increment of the suction parameter. However, the change in the mixed convection parameter has little effect on the local Nusselt number. The acquired behaviors of the physical quantities of interest may be influenced by the changes in temperature ($-\theta'(0)$) and velocity ($f''(0)$) gradients at the cone/wedge wall when the suction and mixed convection parameters are varied. Additionally, the cone geometry exhibits a lower local skin friction coefficient and higher local Nusselt number than the wedge geometry.

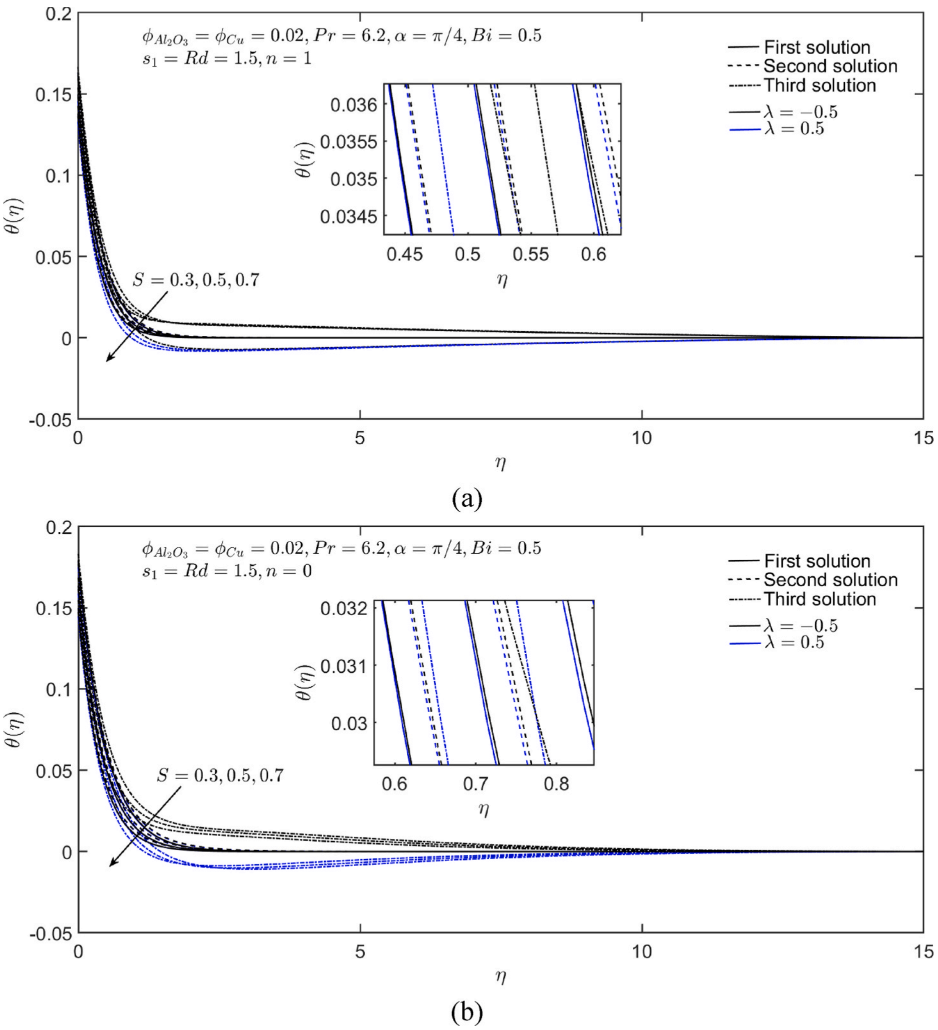

Fig. 5. Temperature profiles for (a) cone and (b) wedge with varying values of the suction parameter.

Next, the effects of suction are depicted in Figs. 4 and 5. The velocity profiles in Fig. 4 show a decrement behavior as S increases. The same behavior is noted for the temperature profile in Fig. 5. In these figures, the thickness of the boundary layer decreases as the suction parameter increases. The thinning of the boundary layers helps stabilize the boundary layer and delay the transition to turbulent flow [56]. Generally, suction draws the hybrid nanofluid closer to the cone/wedge surface. Low-momentum fluid in close proximity to the surface is then removed through suction. Thus, the momentum and thermal boundary layers diminish. Consequently, the velocity gradient (($f''(0)$)) decreases while the temperature gradient ($-\theta'(0)$) increases at the cone/wedge surface. Then, the local skin friction coefficient $\left(Re_x^{\frac{1}{2}}C_f = \frac{\mu_{hnf}}{\mu_{H_2O}} f''(0)\right)$ decreases while the local Nusselt number $\left(Re_x^{-\frac{1}{2}}Nu_x = -\left(\frac{k_{hnf}}{k_{H_2O}} + \frac{4}{3}Rd\right)\theta'(0)\right)$ increases with the increasing suction parameter, as obtained in Figs. 2 and 3.

Then, the effects of the Biot number (Bi) on the local Nusselt number and temperature profile are presented in Table 5 and Fig. 6, respectively. The increase in the Biot number raises the local Nusselt number for assisting and opposing flows (see Table 5). Similarly, the temperature profile also increases with the Biot number, as shown in Fig. 6. The Biot number is defined as the ratio of heat convection at the surface to heat conduction within the surface [43]. Hence, the rise in the Biot number indicates the enhancement of heat convection from the cone/wedge surface to the surrounding hybrid nanofluid. Consequently, it raises the temperature profile and thickens the thermal boundary layer, as observed in Fig. 6. As the temperature of the cone/wedge surface rises with the Biot number, the temperature gradient at the surface also increases and enhances the local Nusselt number, as obtained in Table 5.

Similarly, the increment of the radiation parameter (Rd) promotes the thickening of the thermal boundary layer and raises the temperature profile, as shown in Fig. 7. Furthermore, the local Nusselt number, listed in Table 5, increases with the radiation parameter. According to Fagbade et al. [57], the large value of Rd provides more heat to the fluid, enhancing the temperature profile

Table 5

The values of $Re_x^{-\frac{1}{2}}Nu_x$ when $Pr = 6.2, \phi_{Al_2O_3} = \phi_{Cu} = 0.02, \alpha = \pi/4$ and $S = 0.5$

n	λ	Bi	Rd	s_1	$Re_x^{-\frac{1}{2}}Nu_x$		
					First solution	Second solution	Third solution
0	−0.5	0.3	1.5	1.5	0.74751	0.74624	0.74206
		0.5	1.3		1.07666	1.07429	1.07022
			1.7		1.25253	1.24855	1.23929
			1.5	1.3	1.15821	1.15511	1.15341
				1.7	1.17184	1.16887	1.15691
				1.5	1.16533	1.16224	1.15563
		0.7			1.53237	1.52700	1.51820
	0.5	0.3	1.5	1.5	0.74762	0.74638	0.75035
		0.5	1.3		1.07695	1.07464	1.07843
			1.7		1.25309	1.24926	1.25768
			1.5	1.3	1.15866	1.15573	1.15642
				1.7	1.17223	1.16933	1.18062
				1.5	1.16575	1.16274	1.16884
		0.7			1.53331	1.52814	1.53606
1	−0.5	0.3	1.5	1.5	0.75500	0.75415	0.75414
		0.5	1.3		1.09256	1.09094	1.08601
			1.7		1.27339	1.27073	1.26428
			1.5	1.3	1.17859	1.17642	1.17281
				1.7	1.18841	1.18638	1.17867
				1.5	1.18367	1.18160	1.17590
		0.7			1.56428	1.56060	1.55308
	0.5	0.3	1.5	1.5	0.75507	0.75422	0.75777
		0.5	1.3		1.09275	1.09114	1.09596
			1.7		1.27374	1.27113	1.27739
			1.5	1.3	1.17887	1.17673	1.18026
				1.7	1.18865	1.18665	1.19415
				1.5	1.18393	1.18185	1.18739
		0.7			1.56487	1.56487	1.56855

and the thermal boundary layer thickness. In addition, it is noticed that the thermal radiation parameter has dominant effects on the local Nusselt number. Despite the decrement in $-\theta'(0)$, the local Nusselt number $\left(Re_x^{-\frac{1}{2}}Nu_x = -\left(\frac{k_{hnf}}{k_f} + \frac{4}{3}Rd\right)\theta'(0)\right)$ still shows improvement due to the increase in the radiation parameter. Therefore, increasing the radiation parameter can boost the heat transfer rate.

As depicted in Fig. 8, the temperature profile and thermal boundary layer thickness decrease as the wall temperature parameter (s_1) increases. Similar behavior has been reported by Dawar et al. [39] and Ramzan et al. [42]. The increase in the wall temperature parameter and the reduction in the temperature profile of the hybrid nanofluid enlarge the temperature gradient at the cone/wedge surface. Consequently, this causes the local Nusselt number to increase, as shown in Table 5. However, the increasing impact of s_1 towards the local Nusselt number is seen to be more significant for the cone compared to the wedge. Besides that, it has been observed that the assisting flow generates a higher local Nusselt number than the opposing flow (see Table 5). Thus, the assisting flow has a greater heat transfer rate.

6. Response surface methodology

Response surface methodology (RSM) is a statistical tool used to determine the relationship and importance of independent variables to a response. In the present study, RSM is employed to find the significant controlling parameters that optimize the local Nusselt number. The optimum condition for the local Nusselt number is achieved when its value is maximized, indicating the highest heat transfer rate between the cone/wedge surface and the ambient fluid.

As discussed in the previous section, the assisting flow outperformed the opposing flow in terms of heat transfer rate. Therefore, only the assisting flow case is considered in this section. Here, the radiation parameter (Rd), wall temperature parameter (s_1), and Biot number (Bi) are treated as the independent variables, while the local Nusselt number $\left(Re_x^{-\frac{1}{2}}Nu_x\right)$ is the response. These independent variables are assigned as A, B, and C, respectively, with their actual values coded as high (1), medium (0), and low (−1). Following the face-centered central composite design, the experimental design consists of 20 runs. The number of runs is determined using the formula $2^N + 2N + P$, where $P(= 6)$ is the center point, and $N(= 3)$ is the number of independent variables [58]. Tables 6 and 7 present the independent variables and their respective response values, calculated at the actual values using the bvp4c solver in MATLAB.

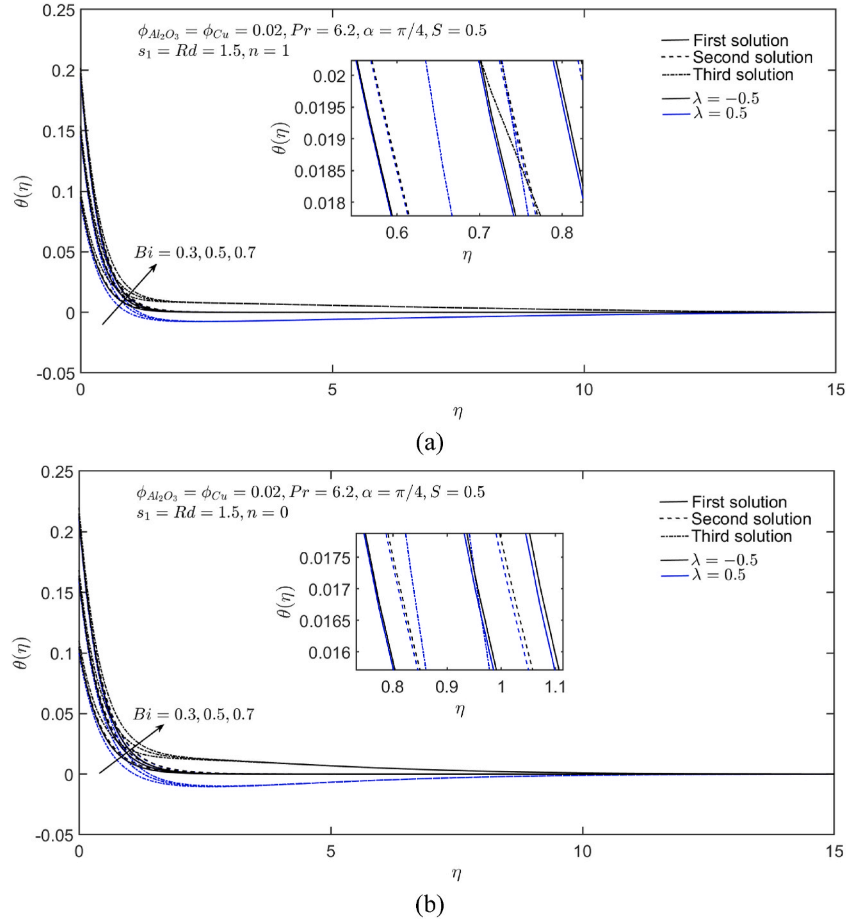

Fig. 6. Temperature profiles for (a) cone and (b) wedge with varying values of Biot number.

In general, the following equation can be used to describe the relationship between the independent variables and the response [59]:

$$\text{Response} = N(\text{A}, \text{B}, \text{C}) \pm Er, \tag{29}$$

with the statistical error (Er) and unknown response function (N). Then, the general quadratic model containing the intercept term (c_0), the linear term (c_i), the quadratic term (c_{ii}), and the bilinear two-factor term (c_{ij}) is expressed as:

$$\text{Response} = c_0 + \sum_{i=1}^{N} c_i x_i + \sum_{i=1}^{N} c_{ii} x_i^2 + \sum_{i=1}^{N-1} \sum_{j=i+1}^{N} c_{ij} x_i x_j. \tag{30}$$

The application of this model enables the evaluation of both the individual and interactive effects of the independent variables on the response. In the current study, the quadratic model is given by:

$$\text{Response} = c_0 + c_1\text{A} + c_2\text{B} + c_3\text{C} + c_{11}\text{AA} + c_{22}\text{BB} + c_{33}\text{CC} + c_{12}\text{AB} + c_{13}\text{AC} + c_{23}\text{BC}. \tag{31}$$

Next, an analysis of variance (ANOVA) is carried out to eliminate any insignificant term from correlation (31). The insignificant term is decided through a p-value > 0.05 (95 % significance level). Based on the ANOVA, the terms AA, BB, and AB for the assisting flow over the cone/wedge are found to be insignificant to correlation (31). Upon eliminating these terms, we repeated the ANOVA to confirm the significance of the remaining terms, and the results are tabulated in Tables 8 and 9. The new correlations, containing only the statistically significant terms, are expressed as follows:

i) Cone

$$\text{Response} = 1.18376 + 0.08819\text{ A} + 0.00520\text{ B} + 0.40448\text{ C} - 0.02450\text{ CC} + 0.02748\text{ AC} + 0.00328\text{ BC}. \tag{32}$$

ii)Wedge

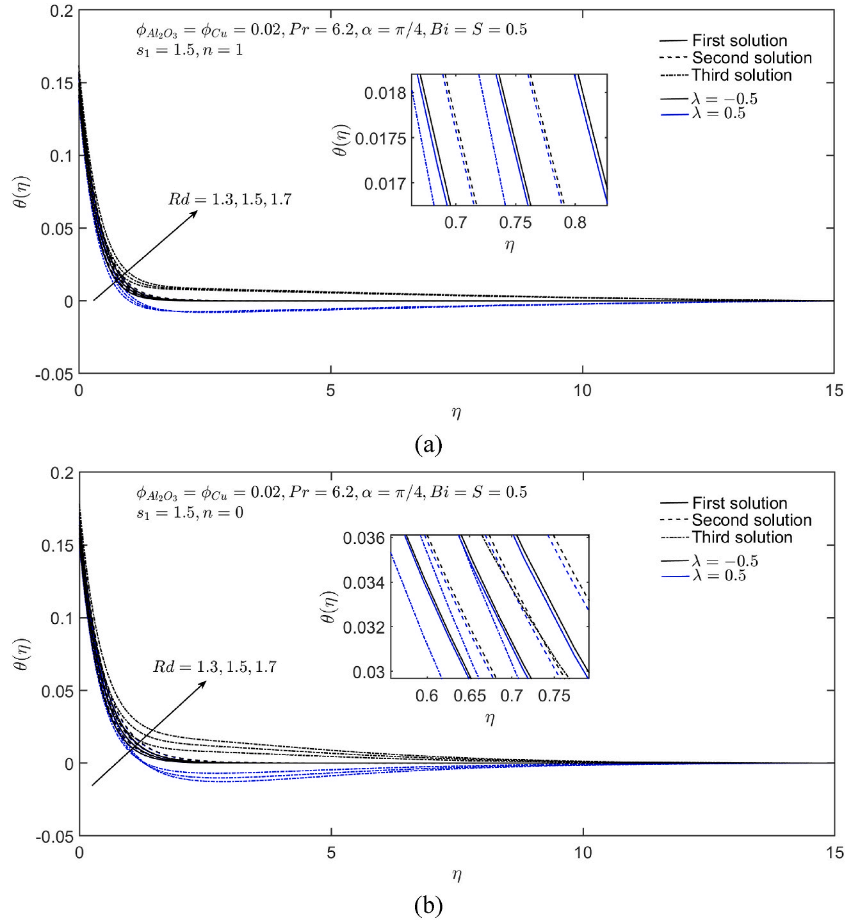

Fig. 7. Temperature profiles for (a) cone and (b) wedge with varying values of radiation parameter.

$$\text{Response} = 1.16554 + 0.08567\text{ A} + 0.00718\text{ B} + 0.39235\text{ C} - 0.02594\text{ CC} + 0.02599\text{ AC} + 0.00447\text{ BC}. \quad (33)$$

Then, the interactive effects of the independent variables on the response are analyzed from the contour and surface plots displayed in Figs. 9 and 10. It can be observed from the plots that the independent variable A is more dominant than B in increasing the response. The response improves by raising the value of A in the presence of any value of B. Hence, the radiation parameter (A) is considered superior to the wall temperature parameter (B) in enhancing the local Nusselt number (response) and heat transfer rate. However, A loses its dominance when interacting with C. The Biot number (C) outperforms the radiation parameter (A) in increasing the local Nusselt number (response). Furthermore, when B and C interact, the response increases exclusively with C. Therefore, we can deduce that the Biot number (C) has the most significant influence on improving the local Nusselt number (response), followed by the radiation parameter (A) and the wall temperature parameter (B).

Finally, the optimization results are presented in Tables 10 and 11. The results indicate that the largest local Nusselt number, corresponding to the highest heat transfer rate, can be achieved at high values of the Biot number, radiation parameter, and wall temperature parameter. Based on these tables, it is estimated that.

i. For the assisting flow over a cone, with a desirability of 99.96 %, the local Nusselt number is maximized at 1.68790.
ii. For the assisting flow over a wedge, with a desirability of 99.92 %, the local Nusselt number is maximized at 1.65526.

These maximized values of the local Nusselt number are obtained at $Rd = 1.7$ (A), $s_1 = 1.7$ (B), and $Bi = 0.7$ (C).

7. Conclusion

The steady flow of a hybrid nanofluid over a permeable, non-isothermal cone/wedge is analyzed with the effects of thermal radiation, mixed convection, and convective boundary condition. Governing partial differential equations and boundary conditions are utilized to describe the flow problem mathematically. Then, these equations are converted into non-linear ordinary differential equations through similarity transformations and solved using the bvp4c solver. The stability analysis revealed that only the first

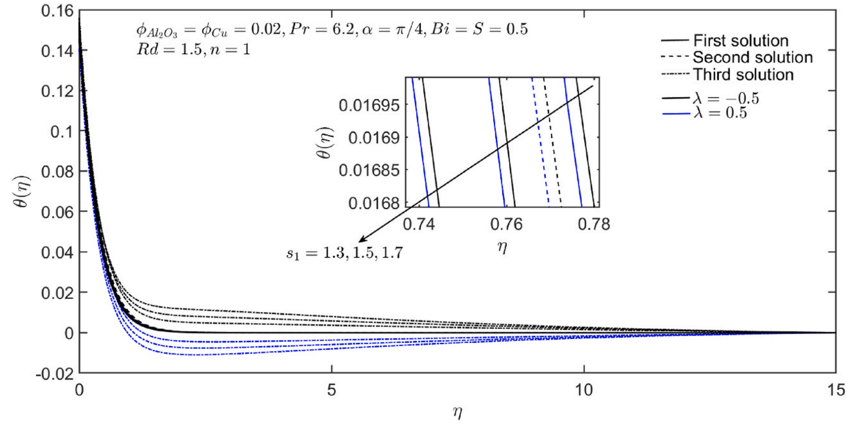

(a)

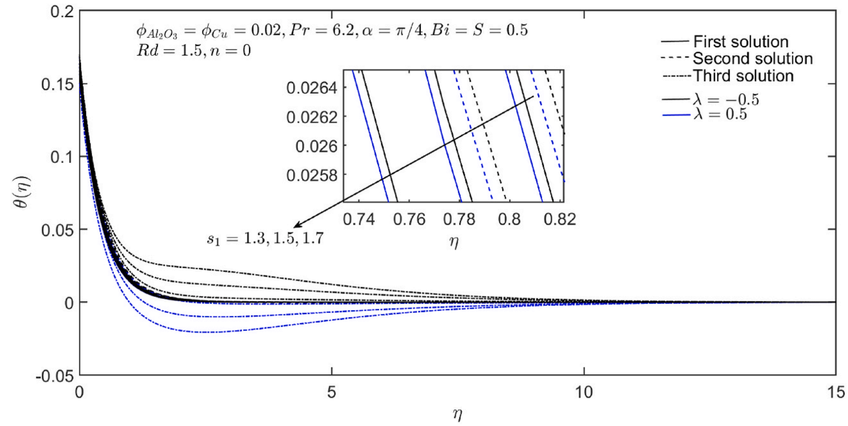

(b)

Fig. 8. Temperature profiles for (a) cone and (b) wedge with varying values of wall temperature parameter.

Table 6

Values of $Re_x^{-\frac{1}{2}}Nu_x$ at $Pr = 6.2, \phi_{Al_2O_3} = \phi_{Cu} = 0.02, n = 1, \lambda = S = 0.5,$ and $\alpha = \pi/4$ (assisting flow for cone).

Runs	Actual values			Coded			Response
	Rd	s_1	Bi	A	B	C	$Re_x^{-1/2}Nu_x$
1	1.3	1.3	0.3	−1	−1	−1	0.69287
2	1.7	1.3	0.3	1	−1	−1	0.81254
3	1.3	1.7	0.3	−1	1	−1	0.69626
4	1.7	1.7	0.3	1	1	−1	0.81715
5	1.3	1.3	0.7	−1	−1	1	1.44099
6	1.7	1.3	0.7	1	−1	1	1.66880
7	1.3	1.7	0.7	−1	1	1	1.45573
8	1.7	1.7	0.7	1	1	1	1.68831
9	1.3	1.5	0.5	−1	0	0	1.09275
10	1.7	1.5	0.5	1	0	0	1.27374
11	1.5	1.3	0.5	0	−1	0	1.17887
12	1.5	1.7	0.5	0	1	0	1.18865
13	1.5	1.5	0.3	0	0	−1	0.75507
14	1.5	1.5	0.7	0	0	1	1.56487
15	1.5	1.5	0.5	0	0	0	1.18393
16	1.5	1.5	0.5	0	0	0	1.18393
17	1.5	1.5	0.5	0	0	0	1.18393
18	1.5	1.5	0.5	0	0	0	1.18393
19	1.5	1.5	0.5	0	0	0	1.18393
20	1.5	1.5	0.5	0	0	0	1.18393

Table 7
Values of $Re_x^{-\frac{1}{2}}Nu_x$ at $Pr = 6.2, \phi_{Al_2O_3} = \phi_{Cu} = 0.02, n = 0, \lambda = S = 0.5,$ and $\alpha = \pi/4$ (assisting flow for wedge).

Runs	Actual values			Coded			Response
	Rd	s_1	Bi	A	B	C	$Re_x^{-1/2}Nu_x$
1	1.3	1.3	0.3	−1	−1	−1	0.68571
2	1.7	1.3	0.3	1	−1	−1	0.80302
3	1.3	1.7	0.3	−1	1	−1	0.69047
4	1.7	1.7	0.3	1	1	−1	0.80949
5	1.3	1.3	0.7	−1	−1	1	1.41044
6	1.7	1.3	0.7	1	−1	1	1.62928
7	1.3	1.7	0.7	−1	1	1	1.43068
8	1.7	1.7	0.7	1	1	1	1.65606
9	1.3	1.5	0.5	−1	0	0	1.07695
10	1.7	1.5	0.5	1	0	0	1.25309
11	1.5	1.3	0.5	0	−1	0	1.15866
12	1.5	1.7	0.5	0	1	0	1.17223
13	1.5	1.5	0.3	0	0	−1	0.74762
14	1.5	1.5	0.7	0	0	1	1.53331
15	1.5	1.5	0.5	0	0	0	1.16575
16	1.5	1.5	0.5	0	0	0	1.16575
17	1.5	1.5	0.5	0	0	0	1.16575
18	1.5	1.5	0.5	0	0	0	1.16575
19	1.5	1.5	0.5	0	0	0	1.16575
20	1.5	1.5	0.5	0	0	0	1.16575

Table 8
ANOVA after eliminating AA, BB, and AB (assisting flow for cone).

Source	DF	Adj SS	Adj MS	F-Value	P-Value
Model	6	1.72323	0.28720	170111.78363	0.00000
Linear	3	1.71410	0.57137	338421.38515	0.00000
A	1	0.07778	0.07778	46070.25797	0.00000
B	1	0.00027	0.00027	160.34308	0.00000
C	1	1.63605	1.63605	969033.55440	0.00000
Square	1	0.00300	0.00300	1777.64378	0.00000
CC	1	0.00300	0.00300	1777.64378	0.00000
2-Way Interaction	2	0.00613	0.00306	1814.45127	0.00000
AC	1	0.00604	0.00604	3577.88598	0.00000
BC	1	0.00009	0.00009	51.01656	0.00001
Error	13	0.00002	0.00000		
Lack-of-Fit	8	0.00002	0.00000	*	*
Pure Error	5	0.00000	0.00000		
Total	19	1.72325			

Table 9
ANOVA after eliminating AA, BB, and AB (assisting flow for wedge).

Source	DF	Adj SS	Adj MS	F-Value	P-Value
Model	6	1.62219	0.27036	119095.49051	0.00000
Linear	3	1.61326	0.53775	236880.41818	0.00000
A	1	0.07339	0.07339	32329.05883	0.00000
B	1	0.00052	0.00052	227.21472	0.00000
C	1	1.53935	1.53935	678084.98098	0.00000
Square	1	0.00336	0.00336	1481.45402	0.00000
CC	1	0.00336	0.00336	1481.45402	0.00000
2-Way Interaction	2	0.00556	0.00278	1225.11725	0.00000
AC	1	0.00540	0.00540	2379.70366	0.00000
BC	1	0.00016	0.00016	70.53084	0.00000
Error	13	0.00003	0.00000		
Lack-of-Fit	8	0.00003	0.00000	*	*
Pure Error	5	0.00000	0.00000		
Total	19	1.62222			

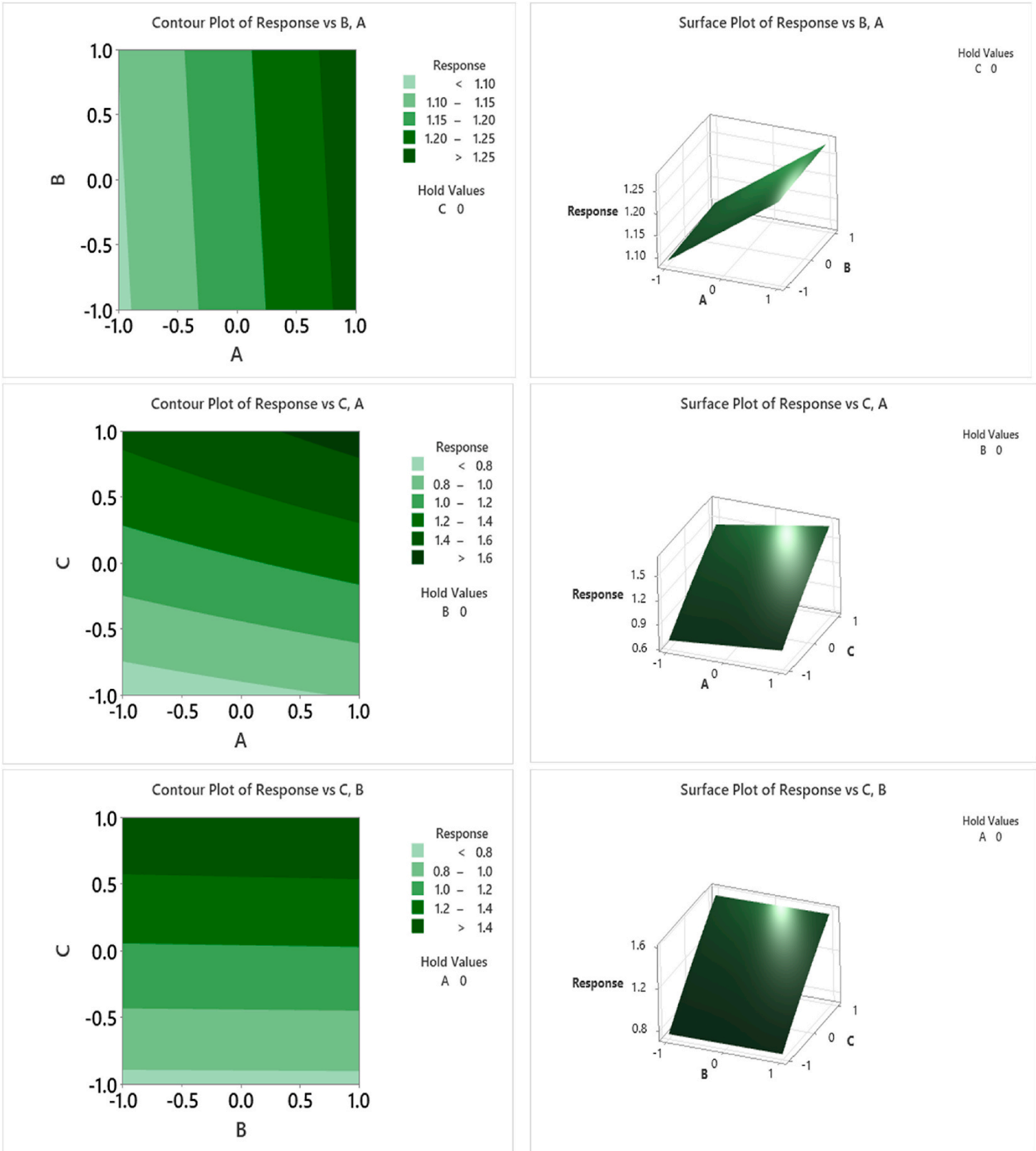

Fig. 9. Contour and surface plots for various interactions of independent variables: Assisting flow for cone.

solution given by the solver is stable. The findings from the first solution are then summarized as follows.

1. The increase in the mixed convection parameter enhances the local skin friction coefficient but has little impact on the local Nusselt number.
2. The local skin friction coefficient for the assisting and opposing flows over the cone and wedge decreases when the suction parameter increases. Conversely, the local Nusselt number increases with the suction parameter.
3. The velocity and temperature profiles decrease as the suction parameter increases.
4. The temperature profile increases with the higher values of the Biot number and radiation parameter but decreases as the wall temperature parameter increases.
5. The hybrid nanofluid flow over the cone geometry has a lower local skin friction coefficient but a higher local Nusselt number than the wedge.
6. The local skin friction coefficient and Nusselt number generated by the assisting flow are greater than the opposing flow.

Meanwhile, the statistical investigation through RSM reveals that the Biot number has the most potent effects on the local Nusselt number, followed by the radiation and wall temperature parameters. With desirability of 99.96 % (cone) and 99.92 % (wedge), the

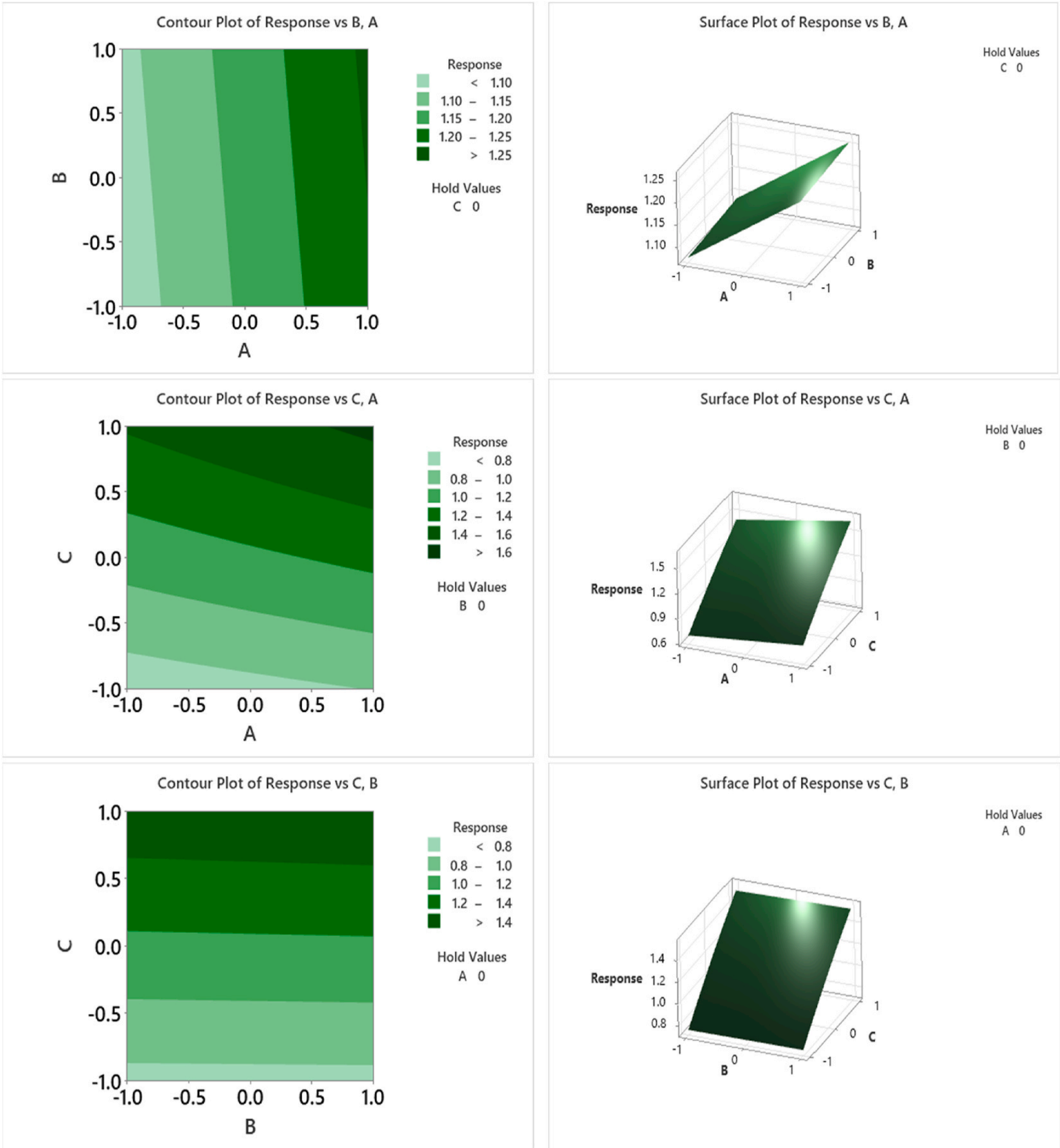

Fig. 10. Contour and surface plots for various interactions of independent variables: Assisting flow for wedge.

Table 10
Optimization (assisting flow for cone).

Solution	A	B	C	Response Fit	Composite Desirability
1	1	1	1	1.68790	0.99959

Table 11
Optimization (assisting flow for wedge).

Solution	A	B	C	Response Fit	Composite Desirability
1	1	1	1	1.65526	0.99918

optimal combination for maximizing the local Nusselt number is found to be $Rd = s_1 = 1.7$ and $Bi = 0.7$, resulting in optimal local Nusselt number of 1.68790 (cone) and 1.65526 (wedge). Setting these parameters at their high levels achieves the highest heat transfer rate for an efficient cooling process in this studied configuration.

Since the present study focuses on the flow of hybrid nanofluid containing spherical-shaped nanoparticles, future work could explore ternary hybrid nanofluid flows with various shapes of nanoparticles. Furthermore, the numerical and statistical results obtained in this study can be validated through experimental investigations. Additional conditions or effects could also be incorporated to extend the applicability of the current flow problem to real-world applications.

CRediT authorship contribution statement

Rusya Iryanti Yahaya: Writing – review & editing, Writing – original draft, Methodology, Formal analysis. **Norihan Md Arifin:** Validation, Supervision. **Mohd Shafie Mustafa:** Writing – review & editing, Validation, Funding acquisition. **Ioan Pop:** Writing – original draft, Methodology, Conceptualization. **Fadzilah Md Ali:** Supervision. **Siti Suzilliana Putri Mohamed Isa:** Supervision.

Declaration of competing interest

The authors declare the following financial interests/personal relationships which may be considered as potential competing interests:Mohd Shafie Mustafa reports financial support was provided by Malaysia Ministry of Higher Education. If there are other authors, they declare that they have no known competing financial interests or personal relationships that could have appeared to influence the work reported in this paper.

Acknowledgment

The authors would like to acknowledge the financial support from the Ministry of Higher Education (MOHE) and Universiti Putra Malaysia through the Fundamental Research Grant Scheme (FRGS) (FRGS/1/2023/STG06/UPM/02/1) and Vote no.:5540632.

Data availability

No data was used for the research described in the article.

References

[1] K. Muhammad, T. Hayat, A. Alsaedi, Squeezed flow of Jeffrey nanomaterial with convective heat and mass conditions, Phys Scr 94 (2019), https://doi.org/10.1088/1402-4896/ab234f.
[2] T. Hayat, K. Muhammad, I. Ullah, A. Alsaedi, S. Asghar, Rotating squeezed flow with carbon nanotubes and melting heat, Phys Scr 94 (2019), https://doi.org/10.1088/1402-4896/aaef66.
[3] K. Muhammad, T. Hayat, A. Alsaedi, B. Ahmad, Numerical study of entropy production minimization in Bödewadt flow with carbon nanotubes, Phys. Stat. Mech. Appl. 550 (2020), https://doi.org/10.1016/j.physa.2019.123966.
[4] T. Hayat, S. Momani Inayatullah, K. Muhammad, FDM analysis for nonlinear mixed convective nanofluid flow with entropy generation, Int. Commun. Heat Mass Tran. 126 (2021), https://doi.org/10.1016/j.icheatmasstransfer.2021.105389.
[5] K. Muhammad, T. Hayat, A. Alsaedi, OHAM analysis of fourth-grade nanomaterial in the presence of stagnation point and convective heat-mass conditions, Waves Random Complex Media 33 (2023), https://doi.org/10.1080/17455030.2021.1892865.
[6] Z. Nisar, T. Hayat, K. Muhammad, B. Ahmed, A. Aziz, Significance of Joule heating for radiative peristaltic flow of couple stress magnetic nanofluid, J. Magn. Magn Mater. 581 (2023), https://doi.org/10.1016/j.jmmm.2023.170951.
[7] J. Sarkar, P. Ghosh, A. Adil, A review on hybrid nanofluids: recent research, development and applications, Renew. Sustain. Energy Rev. 43 (2015), https://doi.org/10.1016/j.rser.2014.11.023.
[8] J.A. Ranga Babu, K.K. Kumar, S. Srinivasa Rao, State-of-art review on hybrid nanofluids, Renew. Sustain. Energy Rev. 77 (2017), https://doi.org/10.1016/j.rser.2017.04.040.
[9] G. Huminic, A. Huminic, Entropy generation of nanofluid and hybrid nanofluid flow in thermal systems: a review, J. Mol. Liq. 302 (2020), https://doi.org/10.1016/j.molliq.2020.112533.
[10] M. Muneeshwaran, G. Srinivasan, P. Muthukumar, C.C. Wang, Role of hybrid-nanofluid in heat transfer enhancement – a review, Int. Commun. Heat Mass Tran. 125 (2021), https://doi.org/10.1016/j.icheatmasstransfer.2021.105341.
[11] M.A. Harun, N.A.C. Sidik, Y. Asako, T.L. Ken, Recent review on preparation method, mixing ratio, and heat transfer application using hybrid nanofluid, Journal of Advanced Research in Fluid Mechanics and Thermal Sciences 95 (2022), https://doi.org/10.37934/arfmts.95.1.4453.
[12] K.V. Modi, P.R. Patel, S.K. Patel, Applicability of mono-nanofluid and hybrid-nanofluid as a technique to improve the performance of solar still: a critical review, J. Clean. Prod. 387 (2023), https://doi.org/10.1016/j.jclepro.2023.135875.
[13] M. Nadeem, I. Siddique, J. Awrejcewicz, M. Bilal, Numerical analysis of a second-grade fuzzy hybrid nanofluid flow and heat transfer over a permeable stretching/shrinking sheet, Sci. Rep. 12 (2022), https://doi.org/10.1038/s41598-022-05393-7.
[14] U. Yashkun, K. Zaimi, N.A. Abu Bakar, A. Ishak, I. Pop, MHD hybrid nanofluid flow over a permeable stretching/shrinking sheet with thermal radiation effect, Int. J. Numer. Methods Heat Fluid Flow 31 (2021), https://doi.org/10.1108/HFF-02-2020-0083.
[15] A. Asghar, T.Y. Ying, Three dimensional mhd hybrid nanofluid flow with rotating stretching/shrinking sheet and joule heating, CFD Lett. 13 (2021), https://doi.org/10.37934/cfdl.13.8.119.
[16] S.M. Mousavi, M.N. Rostami, M. Yousefi, S. Dinarvand, I. Pop, M.A. Sheremet, Dual solutions for Casson hybrid nanofluid flow due to a stretching/shrinking sheet: a new combination of theoretical and experimental models, Chin. J. Phys. 71 (2021), https://doi.org/10.1016/j.cjph.2021.04.004.
[17] U.S. Mahabaleshwar, A.B. Vishalakshi, H.I. Andersson, Hybrid nanofluid flow past a stretching/shrinking sheet with thermal radiation and mass transpiration, Chin. J. Phys. 75 (2022), https://doi.org/10.1016/j.cjph.2021.12.014.
[18] K. Muhammad, S.A.M. Abdelmohsen, A.M.M. Abdelbacki, B. Ahmed, Darcy-Forchheimer flow of hybrid nanofluid subject to melting heat: a comparative numerical study via shooting method, Int. Commun. Heat Mass Tran. 135 (2022), https://doi.org/10.1016/j.icheatmasstransfer.2022.106160.
[19] A.B. Vishalakshi, R. Mahesh, U.S. Mahabaleshwar, A.K. Rao, L.M. Pérez, D. Laroze, MHD hybrid nanofluid flow over a stretching/shrinking sheet with skin friction: effects of radiation and mass transpiration, Magnetochemistry 9 (2023) 118, https://doi.org/10.3390/magnetochemistry9050118.

[20] A. Tassaddiq, S. Khan, M. Bilal, T. Gul, S. Mukhtar, Z. Shah, E. Bonyah, Heat and mass transfer together with hybrid nanofluid flow over a rotating disk, AIP Adv. 10 (2020), https://doi.org/10.1063/5.0010181.
[21] M. Ramzan, T. Mehmood, H. Alotaibi, H.A.S. Ghazwani, T. Muhammad, Comparative study of hybrid and nanofluid flows amidst two rotating disks with thermal stratification: statistical and numerical approaches, Case Stud. Therm. Eng. 28 (2021), https://doi.org/10.1016/j.csite.2021.101596.
[22] M. Bilal, A. Saeed, Numerical computation for the dual solution of Sisko hybrid nanofluid flow through a heated shrinking/stretching porous disk, Int. J. Ambient Energy 43 (2022), https://doi.org/10.1080/01430750.2022.2111351.
[23] W. Ibrahim, D. Gamachu, Entropy generation in radiative magneto-hydrodynamic mixed convective flow of viscoelastic hybrid nanofluid over a spinning disk, Heliyon 8 (2022) e11854, https://doi.org/10.1016/j.heliyon.2022.e11854.
[24] R.I. Yahaya, N. Md Arifin, I. Pop, F. Md Ali, S.S.P. Mohamed Isa, Dual solutions for MHD hybrid nanofluid stagnation point flow due to a radially shrinking disk with convective boundary condition, Int. J. Numer. Methods Heat Fluid Flow 33 (2023), https://doi.org/10.1108/HFF-05-2022-0301.
[25] N. Vijay, K. Sharma, Magnetohydrodynamic hybrid nanofluid flow over a decelerating rotating disk with Soret and Dufour effects, Multidiscip. Model. Mater. Struct. 19 (2023), https://doi.org/10.1108/MMMS-08-2022-0160.
[26] C. Sulochana, S.R. Aparna, N. Sandeep, Magnetohydrodynamic MgO/CuO-water hybrid nanofluid flow driven by two distinct geometries, Heat Transfer 49 (2020), https://doi.org/10.1002/htj.21794.
[27] I. Haq, R. Naveen Kumar, R. Gill, J.K. Madhukesh, U. Khan, Z. Raizah, S.M. Eldin, N. Boonsatit, A. Jirawattanapanit, Impact of homogeneous and heterogeneous reactions in the presence of hybrid nanofluid flow on various geometries, Front. Chem. 10 (2022), https://doi.org/10.3389/fchem.2022.1032805.
[28] M.B. Rekha, I.E. Sarris, J.K. Madhukesh, K.R. Raghunatha, B.C. Prasannakumara, Activation energy impact on flow of AA7072-AA7075/water based hybrid nanofluid through a cone, wedge and plate, Micromachines 13 (2022), https://doi.org/10.3390/mi13020302.
[29] T.H. Al-Arabi, A. Mahdy, A.M. Rashad, W. Saad, H.A. Nabwey, Convective flow of a Williamson hybrid nanofluid in a porous medium through a cone and wedge with the effect of the shape of nanoparticles, Heat Transfer 51 (2022), https://doi.org/10.1002/htj.22634.
[30] M. Bilal, I. Ullah, M.M. Alam, W. Weera, A.M. Galal, Numerical simulations through pcm for the dynamics of thermal enhancement in ternary mhd hybrid nanofluid flow over plane sheet, cone, and wedge, Symmetry (Basel) 14 (2022), https://doi.org/10.3390/sym14112419.
[31] M. Yaseen, S.K. Rawat, N.A. Shah, M. Kumar, S.M. Eldin, Ternary hybrid nanofluid flow containing gyrotactic microorganisms over three different geometries with cattaneo–christov model, Mathematics 11 (2023), https://doi.org/10.3390/math11051237.
[32] A. Dawar, S. Islam, Z. Shah, S.A. Lone, A comparative analysis of the magnetized sodium alginate-based hybrid nanofluid flows through cone, wedge, and plate, ZAMM Zeitschrift Fur Angewandte Mathematik Und Mechanik 103 (2023), https://doi.org/10.1002/zamm.202200128.
[33] N.A. Zainal, I. Waini, N.S. Khashi'ie, R. Nazar, I. Pop, MHD hybrid nanofluid flow past a stretching/shrinking wedge with heat generation/absorption impact, CFD Lett. 16 (2024), https://doi.org/10.37934/cfdl.16.6.146156.
[34] S.S.K. Raju, P. Durgaprasad, J.L. Díaz Palencia, A. Wakif, C.S.K. Raju, M. Dinesh kumar, A.N. Muneerah, J.C. Ali, Contour analysis for heat transfer rate in a wedge geometry with non-uniform shapes nanofluid: gradient descent machine learning technique, Results in Engineering 23 (2024) 102714, https://doi.org/10.1016/j.rineng.2024.102714.
[35] I. Waini, A. Ishak, I. Pop, Hybrid nanofluid flow over a permeable non-isothermal shrinking surface, Mathematics 9 (2021), https://doi.org/10.3390/math9050538.
[36] C.H. Chen, Heat transfer characteristics of a non-isothermal surface moving parallel to a free stream, Acta Mech. 142 (2000), https://doi.org/10.1007/BF01190018.
[37] M. Kumari, G. Nath, Non-Darcy mixed convection in power-law fluids along a non-isothermal horizontal surface in a porous medium, Int. J. Eng. Sci. 42 (2004), https://doi.org/10.1016/S0020-7225(03)00140-X.
[38] A.K. Ray, B. Vasu, P.V.S.N. Murthy, O.A. Bég, R.S.R. Gorla, Homotopy semi-numerical modeling of non-Newtonian nanofluid transport external to multiple geometries using a revised buongiorno model, Inventions 4 (2019), https://doi.org/10.3390/inventions4040054.
[39] A. Dawar, Z. Shah, A. Tassaddiq, P. Kumam, S. Islam, W. Khan, A convective flow of Williamson nanofluid through cone and wedge with non-isothermal and non-isosolutal conditions: a revised Buongiorno model, Case Stud. Therm. Eng. 24 (2021), https://doi.org/10.1016/j.csite.2021.100869.
[40] S. Bilal, M. Imtiaz Shah, N.Z. Khan, A. Akgül, K.S. Nisar, Onset about non-isothermal flow of Williamson liquid over exponential surface by computing numerical simulation in perspective of Cattaneo Christov heat flux theory, Alex. Eng. J. 61 (2022), https://doi.org/10.1016/j.aej.2021.11.038.
[41] N. Nithya, B. Vennila, The flow past a non-isothermal shrinking sheet with the effects of thermal radiation and heat source/sink, IAENG Int. J. Appl. Math. 53 (2023).
[42] M. Ramzan, P. Kumam, S.A. Lone, T. Seangwattana, A. Saeed, A.M. Galal, A theoretical analysis of the ternary hybrid nanofluid flows over a non-isothermal and non-isosolutal multiple geometries, Heliyon 9 (2023) e14875, https://doi.org/10.1016/j.heliyon.2023.e14875.
[43] A. Shahzad, F. Liaqat, Z. Ellahi, M. Sohail, M. Ayub, M.R. Ali, Thin film flow and heat transfer of Cu-nanofluids with slip and convective boundary condition over a stretching sheet, Sci. Rep. 12 (2022), https://doi.org/10.1038/s41598-022-18049-3.
[44] B. Takabi, S. Salehi, Augmentation of the heat transfer performance of a sinusoidal corrugated enclosure by employing hybrid nanofluid, Adv. Mech. Eng. 2014 (2014), https://doi.org/10.1155/2014/147059.
[45] N.S. Khashi'ie, I. Waini, M.F. Mukhtar, N.A. Zainal, K. Bin Hamzah, N.M. Arifin, I. Pop, Response surface methodology (rsm) on the hybrid nanofluid flow subject to a vertical and permeable wedge, Nanomaterials 12 (2022), https://doi.org/10.3390/nano12224016.
[46] H.F. Oztop, E. Abu-Nada, Numerical study of natural convection in partially heated rectangular enclosures filled with nanofluids, Int. J. Heat Fluid Flow 29 (2008) 1326–1336, https://doi.org/10.1016/j.ijheatfluidflow.2008.04.009.
[47] S. Rosseland, Astrophysik (1931), https://doi.org/10.1007/978-3-662-26679-3.
[48] A. Ishak, Thermal boundary layer flow over a stretching sheet in a micropolar fluid with radiation effect, Meccanica 45 (2010), https://doi.org/10.1007/s11012-009-9257-4.
[49] E. Magyari, A. Pantokratoras, Note on the effect of thermal radiation in the linearized Rosseland approximation on the heat transfer characteristics of various boundary layer flows, Int. Commun. Heat Mass Tran. 38 (2011), https://doi.org/10.1016/j.icheatmasstransfer.2011.03.006.
[50] R.C. Bataller, Radiation effects for the Blasius and Sakiadis flows with a convective surface boundary condition, Appl. Math. Comput. 206 (2008), https://doi.org/10.1016/j.amc.2008.10.001.
[51] J.H. Merkin, On dual solutions occurring in mixed convection in a porous medium, J. Eng. Math. 20 (1986), https://doi.org/10.1007/BF00042775.
[52] P.D. Weidman, D.G. Kubitschek, A.M.J. Davis, The effect of transpiration on self-similar boundary layer flow over moving surfaces, Int. J. Eng. Sci. 44 (2006) 730–737, https://doi.org/10.1016/j.ijengsci.2006.04.005.
[53] I.S. Awaludin, P.D. Weidman, A. Ishak, Stability analysis of stagnation-point flow over a stretching/shrinking sheet, AIP Adv. 6 (2016) 045308, https://doi.org/10.1063/1.4947130.
[54] I.A. Hassanien, A.A. Abdullah, R.S.R. Gorla, Flow and heat transfer in a power-law fluid over a nonisothermal stretching sheet, Math. Comput. Model. 28 (1998), https://doi.org/10.1016/S0895-7177(98)00148-4.
[55] I. Waini, A. Ishak, I. Pop, Hybrid nanofluid flow over a permeable non-isothermal shrinking surface, Mathematics 9 (2021), https://doi.org/10.3390/math9050538.
[56] M. Brynjell-Rahkola, A. Hanifi, D.S. Henningson, On the stability of a Blasius boundary layer subject to localised suction, J. Fluid Mech. 871 (2019), https://doi.org/10.1017/jfm.2019.326.
[57] A.I. Fagbade, A.J. Omowaye, Influence of thermal radiation on free convective heat and mass transfer past an isothermal vertical oscillating porous plate in the presence of chemical reaction and heat generation-absorption. Boundary Value Problems 2016, 2016, https://doi.org/10.1186/s13661-016-0601-z.
[58] B. Mahanthesh, J. Mackolil, S.M. Mallikarjunaiah, Response surface optimization of heat transfer rate in Falkner-Skan flow of ZnO − EG nanoliquid over a moving wedge: sensitivity analysis, Int. Commun. Heat Mass Tran. 125 (2021), https://doi.org/10.1016/j.icheatmasstransfer.2021.105348.
[59] B. Mahanthesh, K. Thriveni, P. Rana, T. Muhammad, Radiative heat transfer of nanomaterial on a convectively heated circular tube with activation energy and nanoparticle aggregation kinematic effects, Int. Commun. Heat Mass Tran. 127 (2021), https://doi.org/10.1016/j.icheatmasstransfer.2021.105568.